RSC Advances

PAPER

View Article Online
View Journal | View Issue

Cite this: *RSC Adv.*, 2022, **12**, 27189

Band alignment of ZnO-based nanorod arrays for enhanced visible light photocatalytic performance†

Jing Wan,[a] Aseel Shaker Al-Baldawy,[b] Shanzhi Qu,[a] Jinshen Lan,[a] Xiaofang Ye,[a] Yuchen Fei,[a] Jingtian Zhao,[a] Ziyun Wang,[a] Rongdun Hong,[a] Shengshi Guo,[a] Shengli Huang,*[a] Shuping Li*[a] and Junyong Kang[a]

Received 27th June 2022
Accepted 14th September 2022

DOI: 10.1039/d2ra03940k

rsc.li/rsc-advances

A ternary semiconductor ZnO/MoS_2/Ag_2S nanorod array in an intimate core–shell structure was synthesized on glass substrates. The physicochemical properties and photocatalytical performance of the specimen were characterized and compared with single ZnO and binary ZnO/Ag_2S and ZnO/MoS_2 nanorod arrays. It is found that the coating layers depressed the band edge emission of the ZnO core, improved light absorption in the visible range, reduced charge transfer resistance, and increased photocatalytic activity. The ternary heterojunction nanorod array possessed full solar absorption with an efficiency of 52.88% for the degradation of methylene blue under visible light in 30 min. The efficiency was higher than other arrays and was 7.6 times that of the ZnO array. Theory analysis revealed that the coating layer brought different band alignment in the heterojunctions for efficient charge separation and conduction, which was beneficial for the photocatalytic performance.

1. Introduction

With rapid industrialization, hazardous wastes including toxic contaminated air and organic waste water are becoming a serious environmental problem. Semiconductor photocatalysis is regarded as an effective technique to eliminate the pollutants in air and waste water.[1,2] Because of the special energy band structure, the electrons in the valence band (VB) of the semiconductors are excited to the conduction band (CB), leaving holes in the VB when the energy of the incident photons is larger than the bandgap. The charges transfer to the surface and initiate a series of redox reactions. In water containing organic pollutants, the charges will react with H_2O and O_2 to generate strongly oxidizing radicals, such as $\cdot OH$ and $\cdot O_2^-$, which can directly decompose organic pollutants into CO_2, H_2O and other small molecules to achieve the degradation of pollutants.[3]

The semiconductors with good photovoltaic properties, high energy conversion efficiency and excellent physicochemical properties have received extensive attention, among which ZnO is a promising candidate. The ZnO has a direct bandgap of 3.37 eV at room temperature, which owns a strong ability to absorb ultraviolet (UV) light. In addition, the characteristics of non-toxicity, strong stability and low cost make ZnO nanomaterials widely used in photocatalysts, light-emitting diodes, solar cells, gas sensors, and varistors. However, the wide bandgap limits its photocatalytic activity under visible light, and its high exciton binding energy (60 meV) leads to a high electron–hole recombination rate.[4,5] The key to improve photocatalytic activity of ZnO is to achieve efficient spatial separation and rapid transfer of photogenerated charges to surface reaction sites. Constructing an intimate electric field at the catalyst interface is an effective way to achieve maximum carrier separation. The photogenerated charges are transferred under the driving fore of the electric field, which greatly accelerates the separation of electron–hole pairs.[6–8] As visible light occupies approximately 43% of the incoming solar energy, developing efficient photocatalysts capable of harvesting visible sunlight is of great significance from a practical point of view.[9] Combining ZnO with narrow bandgap semiconductors to form heterojunction nanostructures may broaden the light absorption range, separate electrons and holes efficiently, and present excellent functionalities.[10,11] Furthermore, in contrast to a single or binary compound, the assembly of multi-junctions with continuous change of band gap, band alignment, absorption coefficient and crystal structure may prominently improve photoelectric conversion and photocatalytic performance.[12]

---

[a] *Engineering Research Center of Micro-nano Optoelectronic Materials and Devices, Ministry of Education, Fujian Key Laboratory of Semiconductor Materials and Applications, CI Center for OSED, Department of Physics, Jiujiang Research Institute, Xiamen University, Xiamen 361005, China. E-mail: lsp@xmu.edu.cn; huangsl@xmu.edu.cn*

[b] *Department of Food Science, Faculty of Agriculture, University of Kufa, Kufa, Najaf 054003, Iraq*

† Electronic supplementary information (ESI) available: PL spectra at the excitation wavelength of 400 nm, Raman spectra, Tauc plots of the absorption spectra, absorption spectra of degraded MB aqueous solutions in different periods and different conditions, SEM images of ZnO/MoS_2/Ag_2S nanoarrays before and after photodegradation, Mott–Schottky plots, absorption spectra of the degraded MB solution with different scavengers, and photodegradation efficiency. See **https://doi.org/10.1039/d2ra03940k**

Therefore, the ZnO can be coupled with other semiconductors in special characteristics, such as metal sulphide-based semiconductors with unique physical and chemical properties.[13] For example, MoS_2 has a two-dimensional layered structure similar to graphene and transition from an indirect to direct bandgap semiconductor by changing the layer number, in which the value of bandgap (E_g) can be turned from 1.29 to 1.90 eV.[14] While Ag_2S is a narrow bandgap semiconductor ($E_g \approx 1.0$ eV) with broad and strong light absorption in the entire solar spectrum, and has attracted great attention as a potential photocatalyst or photosensitizer.[15,16] The alliance of ZnO nanomaterials with the metal sulphides may bring special properties and functionalities.

With above consideration, ternary semiconductor heterojunction $ZnO/MoS_2/Ag_2S$ nanorod array was synthesized on the conductive fluorine-doped tin oxide (FTO) glass substrates. The physicochemical properties and photocatalytic performance of the specimen were characterized and compared with single semiconductor ZnO and binary semiconductor heterojunction ZnO/MoS_2 and ZnO/Ag_2S nanorod arrays. It is found that the nanorods were well aligned vertically on the FTO substrate. The MoS_2 nanosheets and Ag_2S quantum dots adhered tightly on the ZnO nanorod surface, forming an intimate core–shell structure with a strong engineered chemical state for the binary and ternary semiconductor heterojunction arrays. The core–shell nanorod arrays presented weak bandedge emission of the ZnO, strong light absorption in the visible range, low electric resistance, and high photocatalysis under visible light, especially for the $ZnO/MoS_2/Ag_2S$ arrays. The special properties were well analyzed by the band alignment.

2. Experimental

2.1 Chemical reagents

Conductive fluorine-doped tin oxide (FTO) glass substrates (KVFTO-P003) were purchased from Zhuhai Kaivo Optoelectronic Technology Co., Ltd (Guangdong, China). Diethyl zinc ($Zn(C_2H_5)_2$, 99.999%) for atomic layer deposition (ALD) was bought from Ke-Micro Company (Jiaxing, China). Silver nitrate ($AgNO_3$, 99.95%) was ordered from the First Reagent Factory (Shanghai, China). Methylene blue (MB, 98.5%), zinc acetate dihydrate ($Zn(CH_3COO)_2 \cdot 2H_2O$, 99%), sodium sulfide nonahydrate ($Na_2S \cdot 9H_2O$, 98%), isopropanol (IPA, 99.7%), and ammonium oxalate (AO, 99.5%), and hexamethylenetetramine($C_6H_{12}N_4$, 99.5%) were all bought from Xilong Chemical Co. Ltd (Guangdong, China). Octylamine (99%) was ordered from Jizhi Biochemical Technology Co., Ltd (Shanghai, China). Molybdenum trioxide (MoO_3, 99.99%) was purchased from Xiamen Senkesi Technology Co., Ltd. Benzoquinone (BQ, 97%) was ordered from Aladdin Co. Ltd (Shanghai, China). Sulfur powder (99.99%) was bought from Xiamen Luyin Reagent Co., Ltd. Distilled water (H_2O) with a resistivity higher than 18.0 MΩ cm was supplied by a Hi-tech laboratory water purification system. All the solvents and chemicals used in the experiments were at least reagent grade and were used as received.

2.2 Synthesis of semiconductor nanorod arrays

The ZnO nanorod arrays were fabricated on FTO substrates by a hydrothermal method,[17] while the MoS_2 and Ag_2S coating layers were synthesized, respectively by a solvothermal method[18] and a successive ionic-layer adsorption and reaction (SILAR) process.[19] Specifically, for the ZnO nanorod arrays, a layer of ZnO seed layer in 30 nm thickness was deposited on the cleaned FTO substrates by a TALD-100-2H1R ALD system from Ke-Micro Company (Jiaxing, China). Afterwards, the substrates were inverted in the solution containing 20 mM $Zn(CH_3COO)_2 \cdot 2H_2O$ and 20 mM $C_6H_{12}N_4$ at 90 °C for 80 min to grow the ZnO nanorods. For the ZnO/MoS_2 nanorod arrays, 0.07 g of MoO_3 and 0.035 g of sulfur powders were added into 10 mL of octylamine under magnetic stirring. 12 mL of absolute ethanol was poured into the mixed solution. After about 5 min, the solution turned to a light-yellow suspension, which was then moved into a Teflon-lined autoclave. The ZnO nanorod arrays on FTO glass substrate was immersed in the suspension, where the ZnO side faced downward. The autoclave was sealed and stored in a muffle furnace at 190 °C for 2 h, and finally cooled naturally to room temperature. The substrate was taken out, washed several times with absolute ethanol and deionized water, and dried under nitrogen gas in a slow flow for accelerating evaporation of the cleaning agents without introducing impurities. While for the Ag_2S quantum dots, the nanorod samples were immersed in the solutions successively in a cycle order of 0.1 M $AgNO_3$ 60 s, deionized water 30 s, 0.1 M Na_2S 180 s, deionized water 30 s. The thickness was controlled in 2 cycles of the SILAR process for the ZnO/Ag_2S and $ZnO/MoS_2/Ag_2S$ specimens.

2.3 Characterization

Morphology, structure and chemical composition of the as-synthesized specimens were respectively characterized by a ZEISS Sigma scanning electron microscope (SEM), a Tecnai F30 transmission electron microscope (TEM) at low resolution (LRTEM) and high resolution (HRTEM), two energy dispersive spectroscopes (EDSs) equipped in the SEM and TEM, and an X'Pert PRO X-ray diffractometer (XRD) with Cu Kα radiation ($\lambda =$ 1.54056 Å) respectively. Qualitative and quantitative analysis of elements was executed by a Thermo Scientific ESCALAB 250Xi A1440 X-ray photoelectron spectroscope (XPS). Resonant Raman scattering spectra were performed in back-scattering geometry through a Renishaw LabRAM-HR Raman microscope using 325 nm (He–Cd) laser excitation source. Photoluminescence (PL) spectra were collected on a Hitachi F-7000 fluorescence spectrophotometer with excitation wavelengths of 325 and 400 nm, in which the PMT voltage, scan speed, and slit width were set at 700 V, 240 nm min^{-1}, and 5.0 nm for all the samples. Diffuse reflection spectra and absorption spectra were tested on an Agilent Carry-5000 UV-Vis-NIR spectrophotometer.

2.4 Electrochemical measurement and photocatalytic performance

Electrochemical properties, including AC impedance and photocurrent response, were measured in a three-electrode electrochemical cell by an electrochemical workstation (Chenhua CHI660E, China), with Na_2SO_4 solution (0.1 mol L^{-1}, 200 mL) as electrolyte, the specimens (active area: 1 cm^2) as a working electrode, a platinum plate (area: 1 cm^2) and a Ag/AgCl wire as a counter electrode and a reference electrode, respectively. The AC impedance spectra were measured in a frequency range of 0.01–10^5 Hz at a fixed potential of ~0.3 V. The transient current responses were checked in a 0.1 Hz square wave at a fixed potential of 0.8 V under illumination of different light-emitted diodes (LEDs, 258 nm and 458 nm, 4 mW cm^{-2}). Photocatalytic activity of the samples was evaluated by the degradation of MB solution with a 500 W high-pressure mercury lamp (at the dominant emission wavelengths of 365 nm and $\lambda \geq$ 380 nm, respectively) at ambient temperature. Aqueous suspension of MB solution (5×10^{-6} M) in a volume of 5 mL was poured into a glass Petri dish with a diameter of 32 mm, then a piece of sample was immersed in the solution with the nanorods facing upwards. They were subjected to UV light and simulated sunlight in an intensity of about 1050 μW cm^{-2} and 500 μW cm^{-2}, respectively. The optical absorption intensity of the MB solution was recorded in 30 min interval by the Carry-5000 spectrophotometer. The IPA, BQ and AO were used to trap the free radicals.

3. Results and discussion

Morphology and chemical components of the as-fabricated nanorod arrays were characterized by SEM and EDS, as presented in Fig. 1. The top-view and cross-sectional SEM images reveal that the nanorods are well aligned vertically on the FTO substrate. The ZnO nanorods own a smooth surface with a length of ~1500 nm and a diameter varying in a range of 60–150 nm (see Fig. 1(a1) and (b1)). By coating a layer of Ag_2S (named as ZnO/Ag_2S, see Fig. 1(a2) and (b2)), the rod surface becomes rough with lots of bright quantum dots, and the morphology keeps constant without any deformation. Nevertheless, when the ZnO nanorods are coated by a MoS_2 layer (named as ZnO/MoS_2, see Fig. 1(a3) and (b3)), the rod surface

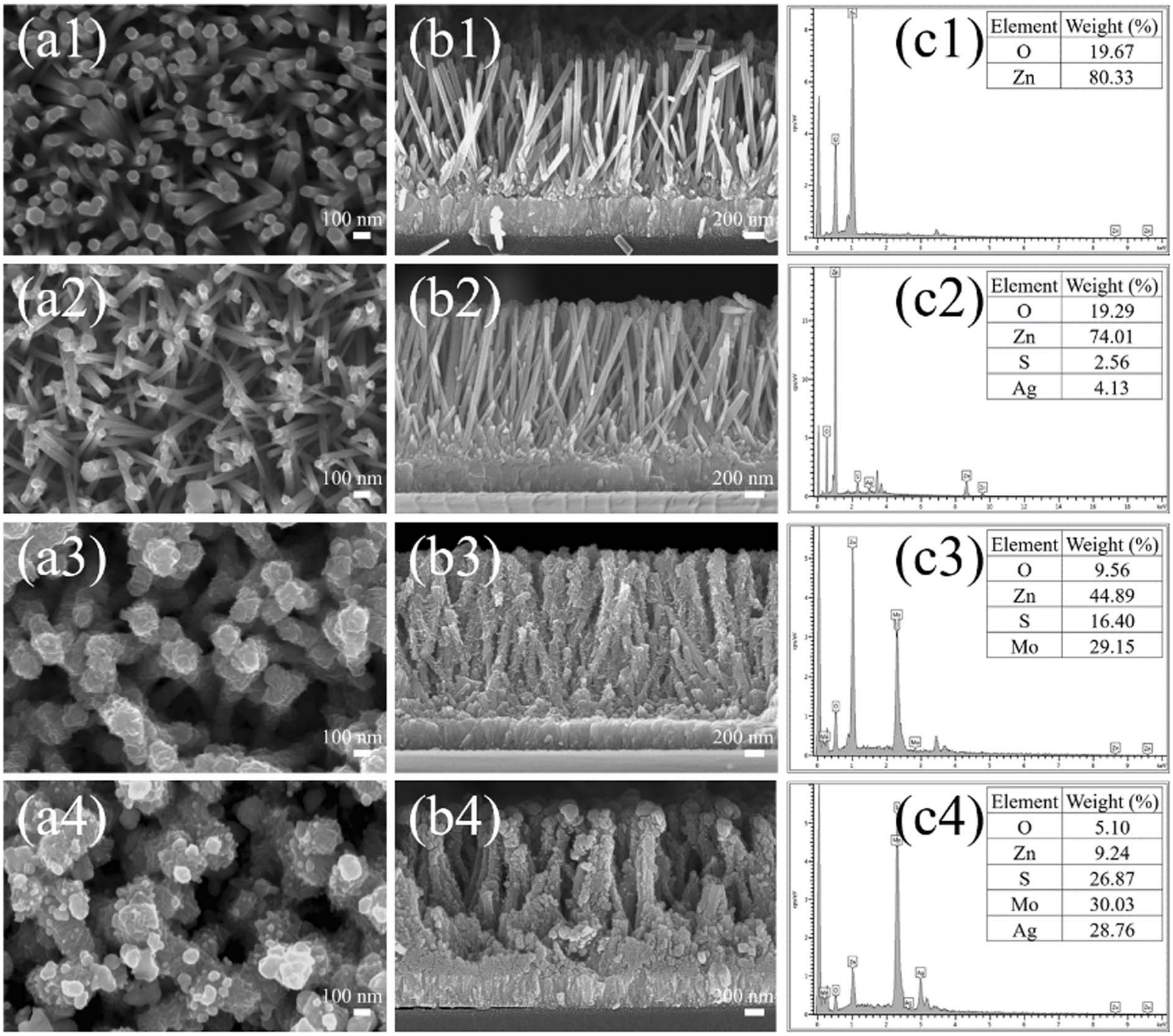

Element	Weight (%)
O	19.67
Zn	80.33

Element	Weight (%)
O	19.29
Zn	74.01
S	2.56
Ag	4.13

Element	Weight (%)
O	9.56
Zn	44.89
S	16.40
Mo	29.15

Element	Weight (%)
O	5.10
Zn	9.24
S	26.87
Mo	30.03
Ag	28.76

Fig. 1 Top-view (a1–a4) and cross-sectional (b1–b4) SEM images and EDS spectra (c1–c4) of the synthesized nanorod arrays: (a1, b1, c1) ZnO, (a2, b2, c2) ZnO/Ag_2S, (a3, b3, c3) ZnO/MoS_2, (a4, b4, c4) ZnO/MoS_2/Ag_2S.

turns wrinkled as the MoS_2 substance exists in a sheet-like structure, and the diameter extends for 100–150 nm. While for the Ag_2S quantum dot-sensitized ZnO/MoS_2 nanorods (named as $ZnO/MoS_2/Ag_2S$, see Fig. 1(a4) and (b4)), a layer of particles in different sizes distribute uniformly on the surface as well as in the gap of the nanosheets. The elemental component of the specimens is confirmed by the EDS spectra without any impurity (see Fig. 1(c1)–(c4)). The weight percentage of Zn element decreases significantly from pure ZnO to the heterogeneous material, especially for the substances with MoS_2 sheets, which is because the central rod is nearly incapsulated by the coating layer.

Core-shell structure of the $ZnO/MoS_2/Ag_2S$ nanorods was investigated by TEM, as displayed in Fig. 2(a) and (b). The intensity profile displays an obvious variation of light contrast of the edge area and dark contrast of the core area (see Fig. 2(a)), confirming formation of the core–shell structure. The shell layer comprises a thin film and lots of small particles in the outside. The film adheres tightly to the core rod without any interspace. The thickness of the film is 47.5 nm, while the diameter of the particles varies in a range of 30–60 nm. The HRTEM image in Fig. 2(b) presents distinct crystal lattice of the shell. The interplanar crystal spacing of the film varies with 0.35 and 0.62 nm, which corresponds to the (004) and (002) planes of the hexagonal MoS_2 (JCPDS no. 37-1492). The lattice spacing of the particle is 0.20 nm, corresponding to the (200) plane of the monoclinic Ag_2S (JCPDS no. 14-0072). Therefore, the ingredients of the specimen as tested by the HRTEM are in good coincident with the EDS in Fig. 1(c4). Fig. 2(c) displays SAED pattern of the shell (the area marked by a yellow circle in the inset), showing polycrystalline diffraction rings of MoS_2 nanosheets and single crystal spots of Ag_2S quantum dots. The SAED pattern in Fig. 2(d) exhibits diffraction lines of the core (the red circle area in the inset), suggesting single crystal of the ZnO. The overall results confirm the presence of a core–shell structure of the heterogeneous $ZnO/MoS_2/Ag_2S$ nanocomposite instead of a physical mixture. The presence of this semiconductor heterojunction might be better for the separation and transferring of photoinduced charges for photocatalytic performance through interfacial bonding.

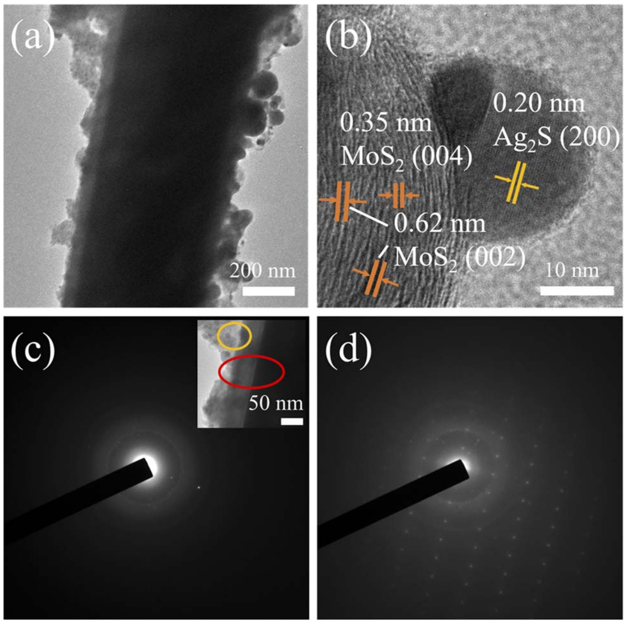

Fig. 2 TEM images and SAED patterns of a $ZnO/MoS_2/Ag_2S$ nanorod: (a) LRTEM image, (b) HRTEM image, and (c, d) SAED patterns. The inset in (c) shows the diffraction area of pattern (c) (in yellow circle) and pattern (d) (in red circle).

Elemental composition and chemical state of the specimens were characterized by XPS. Fig. 3(a) presents survey spectra, demonstrating the presence of corresponding elements in the specimens, in addition to carbon. The carbon content may come from the residual carbon in the hydrothermal solution or the adventitious carbon in the XPS instrument. Fig. 3(b) displays Zn 2p spectra of the specimens. For ZnO nanorods, the two peaks locating at 1022.00 and 1045.00 eV correspond to Zn $2p_{1/2}$ and Zn $2p_{3/2}$, respectively.[20,21] The addition of Ag_2S quantum dots results in a red shift of the peaks to 1021.75 and 1044.81 eV, while the coating of MoS_2 sheets induces a blue shift of the peaks to 1022.70 and 1045.70 eV. The peak position of the $ZnO/MoS_2/Ag_2S$ array is the same as that of the ZnO/MoS_2 array, which may ascribe to the larger content of MoS_2 than Ag_2S. The engineered chemical state of the Zn 2p suggests the strong binding and interaction between the shell and the core. Fig. 3(c) shows XPS spectra of the O 1s. The resonant band can be deconvolved into two peaks, which locate at 530.40 and 531.50 eV for the ZnO array and can be attributed to the O–Zn bonds and oxygen vacancies (or C–O/C=O bonds).[22] After coating the quantum dots and/or nanosheets, the binding energy of the bond and vacancy takes a little change, while their relative intensity ($I_{bond}/I_{vacancy}$) decreases successively from ZnO/Ag_2S to ZnO/MoS_2 and to $ZnO/MoS_2/Ag_2S$, suggesting increasing amount of vacancy or carbon substance. Fig. 3(d) exhibits S 2p spectra of the arrays. Two peaks at 160.40 and 161.63 eV are observed in the ZnO/Ag_2S array, which are in good agreement with S $2p_{3/2}$ and S $2p_{1/2}$ of the Ag_2S quantum dots.[23] The profile of the ZnO/MoS_2 array can be fitted by two sets of doublets, in which a couple at lower energies (163.28 eV for S $2p_{1/2}$ and 162.08 eV for S $2p_{3/2}$) correspond to 1T-phase MoS_2, and another couple at higher energies (164.14 eV for S $2p_{1/2}$ and 162.40 eV for S $2p_{3/2}$) correspond to 2H-phase MoS_2.[18,24] For $ZnO/MoS_2/Ag_2S$ array, the resonant peaks for the Ag_2S and MoS_2 in 1T and 2H phases are also observed. However, the two peaks of the Ag_2S quantum dots blue shift to 161.31 and 162.12 eV, respectively, and the two peaks of the 1T phase blue shift to 163.43 and 162.27 eV, respectively, while the two peaks of the 2H phase remain unchanged. The band intensity of the 1T phase is much stronger than the 2H phase, suggesting that the content of the former phase is much larger than the later phase in the as-prepared ZnO/MoS_2 and $ZnO/MoS_2/Ag_2S$ arrays. The Mo 3d spectra also present a couple of doublets in Fig. 3(e). For ZnO/MoS_2 array, the couple of doublet peaks at 232.40 and 229.28 eV match with Mo $3d_{3/2}$ and $3d_{5/2}$of the 1T-phase MoS_2, and another couple of doublet peaks at higher energies of 233.30 and 230.16 eV match with Mo $3d_{3/2}$ and $3d_{5/2}$ of the 2H-phase MoS_2.[18] Therefore, this observation reveals that the MoS_2 sheets in the ZnO/MoS_2 and $ZnO/MoS_2/Ag_2S$ arrays are

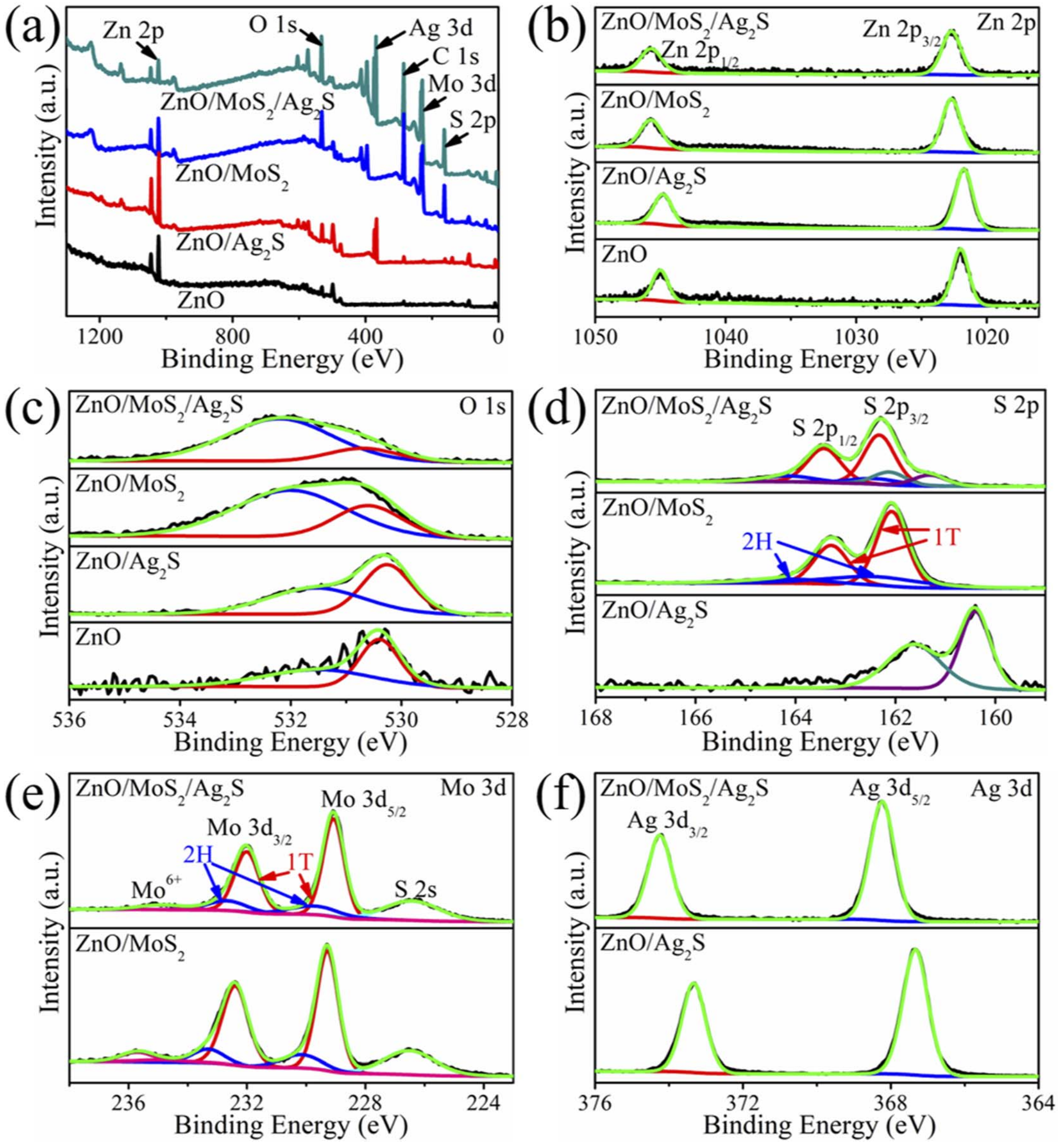

Fig. 3 XPS spectra of the specimens: (a) survey spectrum, (b) Zn 2p, (c) O 1s, (d) S 2p, (e) Mo 3d, and (f) Ag 3d.

composed of mixed 1T and 2H phases, which is coincident with that found in Fig. 3(d). Compared with the ZnO/MoS_2 array, the 1T phase is roughly blue-shifted by 0.2 eV and the 2H phase is stable for the ZnO/MoS_2/Ag_2S array. In addition, a peak at high binding energy of 226.50 eV can be assigned to S 2s, and a peak at 235.70 eV can be attributed to Mo^{6+} of MoO_3 owing to small portion of Mo oxidation.[18] The Ag 3d spectrum of the ZnO/Ag_2S array in Fig. 3(f) shows two peaks at 367.33 eV and 373.33 eV, which can be ascribed to Ag $3d_{5/2}$ and Ag $3d_{3/2}$, respectively.[23] The two peaks blue-shift to 368.23 and 374.25 eV for the ZnO/MoS_2/Ag_2S array, which suggests increasing binding energy of Ag_2S quantum dots for the modulation of the MoS_2 sheets, and the engineered chemical state for the strong interaction in the shell layer.

The crystal structure analysis was also carried out through XRD, as presented in Fig. 4(a). For the ZnO nanorod arrays, except the peaks at 26.61°, 37.95°, 51.78°, 61.87° and 65.94° (2θ) that can be attributed to the FTO substrate (JCPDS Card no. 41-1445), all the other diffraction peaks at 31.77°, 34.42°, 36.25°, 47.54°, 56.60°, 62.86° and 72.56° can be well indexed of the (100), (002), (101), (102), (110), (103) and (004) planes of the wurtzite ZnO crystal (JCPDS Card no. 36-1451). The other specimens possess the ZnO phase, but the XRD patterns do not reveal the existence of Ag_2S and/or MoS_2 phases, which may be due to the thin coating layer or the high content of 1T phase MoS_2.[25,26] Fig. 4(b) shows PL spectra of the samples at the excitation wavelength of 325 nm. The ZnO nanorod arrays display a UV emission at ∼376 nm (3.30 eV), a blue emission at 441 nm (2.81 eV) with a shoulder peak at 410 nm (3.02 eV), and a green emission at 547 nm (2.27 eV). The UV emission is much stronger than the others. As confirmed in the previous research,[27–29] the UV emission originates from bandedge emission for the recombination of free excitons, the blue emissions at 410 and 441 nm derive from transitions from Zn interstitial

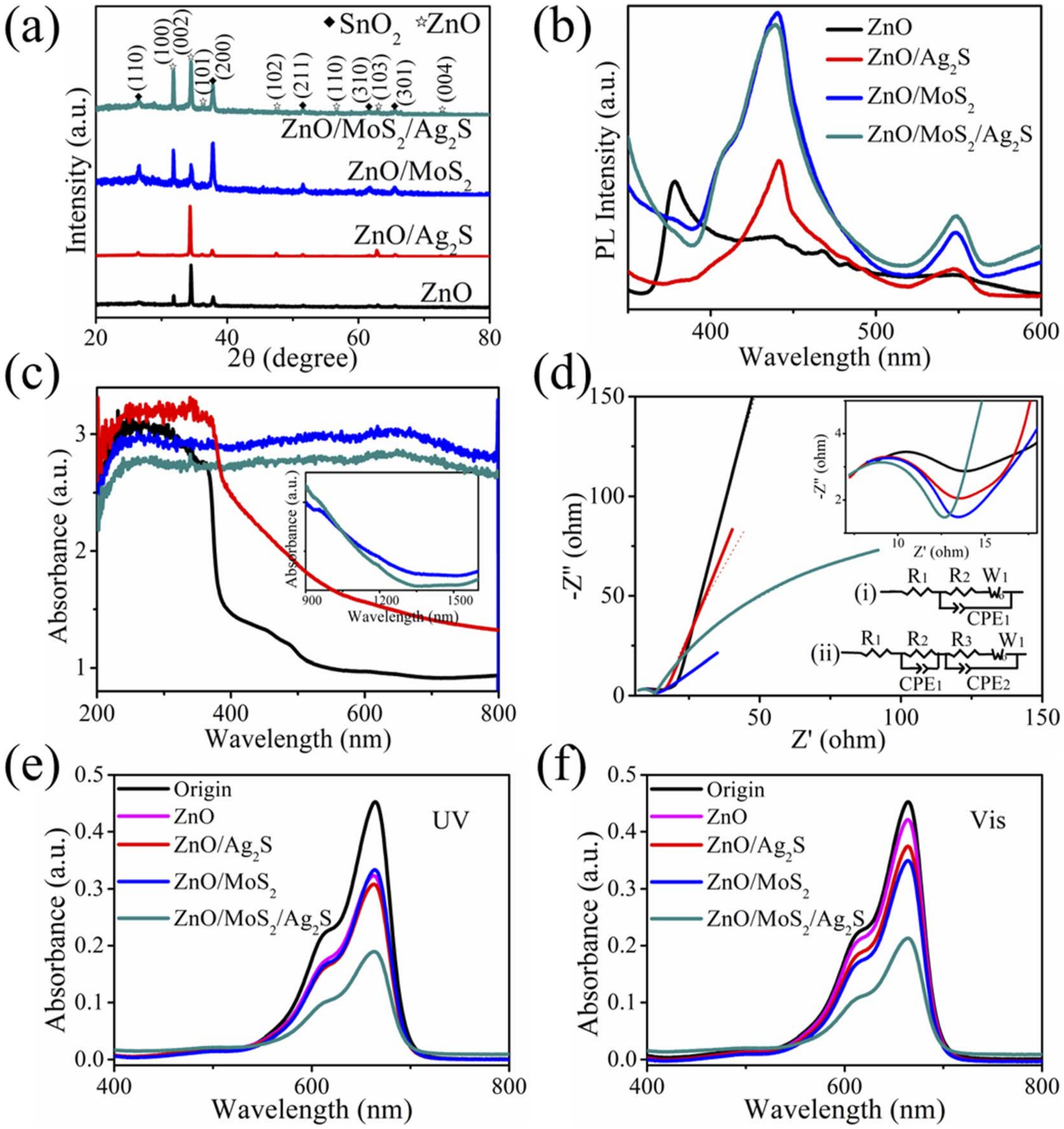

Fig. 4 Optical spectra and photocatalytic performance of the specimens: (a) XRD patterns, (b) PL spectra at an excitation wavelength of 325 nm, (c) absorption spectra, (d) impedance spectra, absorption spectra of the degraded MB aqueous solutions as catalyzed by the specimens under (e) UV light and (f) visible light for 30 min. The dots and solid lines in (d) represent the measured and simulated data, and the insets show the impedance spectra in high-frequency region and the equivalent circuit diagrams.

and extended Zn interstitial states (Zn_i) to the valence band respectively, and the green emission comes from recombination of electrons trapped in the conduction band and deeply trapped holes in oxygen vacancies (Vo). For the heterogeneous nanorod arrays, the bandedge emission is significantly reduced, while the blue and green emissions are distinctly amplified. Nevertheless, the emission bands of the impurities and vacancies are depressed obviously at the excitation of 400 nm (see Fig. S1†). The weakened and vanished emission suggests limited exciton recombination in the heterogeneous specimens, which is advantageous for their potential photovoltaic application. Raman spectra in Fig. S2† display tow resonant bands at 380 and 408 cm^{-1} for ZnO/MoS_2 and $ZnO/MoS_2/Ag_2S$ nanorod arrays, which are the typical in-plane (E^1_{2g}) and out of plane (A_{1g}) vibration modes of individual Mo and S atoms.[30,31] The existence of E^1_{2g} and A_{1g} modes reveals the presence of the MoS_2 sheets.

UV-Vis absorption spectra were carried out to investigate the light response, as shown in Fig. 4(c). The pure ZnO displays a bandedge absorption at 380 nm with low absorption in the visible region. When the ZnO is coupled with Ag_2S to form a binary heterojunction, the absorption edge gets a remarkable red-shift with an obvious enhanced light absorption toward visible range. Moreover, When the ZnO is coupled with MoS_2 to form a binary heterojunction and further coupled with Ag_2S to form a ternary heterojunction, the specimens exhibit a strong and full light absorption in 200–800 nm with an obvious declining in 900–1350 nm. The improved light absorption in visible range may lead to much electron–hole pair separation and enhance photocatalytic activity of the catalysts. The optical bandgap energy (E_g) of the semiconductor catalysts can be calculated from the Tauc plots using the formula:[32]

$$(\alpha h\nu)^{1/n} = A(h\nu - E_g) \quad (1)$$

in which α, h, ν, A and E_g represent the absorption coefficient, Planck's constant, light frequency, proportionality and bandgap energy, respectively, whereas n value is 0.5 for direct semiconductor. The achieved E_g value of ZnO component is 3.33 and 3.23 eV, respectively for the ZnO and ZnO/Ag_2S, while that of the MoS_2 counterpart is 1.18 and 1.16 eV, respectively for the ZnO/MoS_2 and ZnO/MoS_2/Ag_2S (see Fig. S3†). The bandgap energy of ZnO is close to that in PL spectra, but that of the binary and ternary components shows an obvious decrease in contrast to their parent, which is easier for the charge separation by the incident light.

The electrochemical impedance spectroscopy (EIS) was conducted to evaluate conductivity of the samples, as shown in Fig. 4(d). The single and binary components arrays display a semicircle in the high-frequency region and a straight line in the low-frequency region, while the ternary components array show two semicircles. The impedance can be fitted by the equivalent circuit, where diagram (i) for ZnO, ZnO/Ag_2S and ZnO/MoS_2 arrays, and diagram (ii) for ZnO/MoS_2/Ag_2S array. The solid lines are the curves obtained after fitting, and the achieved resistances are shown in Table 1. For the heterojunction nanorod arrays, the solution resistance (R_1) increases, while the charge transfer resistance (R_2) decreases. In comparison with pure ZnO array, the R_2 of ZnO/Ag_2S and ZnO/MoS_2/Ag_2S arrays reduces to be 65% and 64%, respectively, while that of the ZnO/MoS_2 array decreases to be only 41%. This suggests that the heterojunction can not only promote charge separation, but also improve the electrical conductivity, and the MoS_2 sheets play an important role for the contribution.

In order to evaluate photocatalytic activity of the arrays, MB aqueous solutions as catalyzed by different specimen ware examined under visible and UV light. Fig. 4(e) and (f) show absorption spectra of the degraded MB aqueous solutions as catalyzed by different specimens in 30 min. The peak intensity of the degraded solutions is reduced after the photocatalytic process, regardless in visible or UV light, suggesting catalytic ability of the semiconductor specimens. The photodegradation efficiency E can be defined by the following equation,[33]

$$E = (C_0 - C)/C_0 \times 100\% \quad (2)$$

where C_0 and C represent concentration of MB solution pre- and post-degradation, respectively. As the concentration is proportional to the solution absorption,[34] the efficiency is therefore can be calculated by the peak intensity, as supplied in Table 2. Under UV light irradiation, the photocatalytic efficiency is around 30% for the single and binary components. But for ternary components, the efficiency gets 58.12%, nearly twice of other samples. Under visible light irradiation, the efficiency of the ZnO array is only 6.94%, which is much lower than that under UV light for the wide bandgap of ZnO and reduced energy of the incident photons. The incorporation of Ag_2S quantum dots and MoS_2 nanosheets increases the efficiency obviously, and the improvement by MoS_2 nanosheets is greater than that by Ag_2S quantum dots. As a result, the ternary component ZnO/MoS_2/Ag_2S array possesses the highest active catalysis with an efficiency of 52.88%, which is about 7.6 times that of ZnO array and comparable to the efficiencies of the catalysts reported to date (see Table S3†). The result suggests that the formation of ternary semiconductor heterojunctions promotes the photocatalytic efficiency of ZnO, expanding the catalytic application of ZnO-based materials in the visible range.

Table 1 Solution resistance R_1, charge transfer resistance R_2 and bilayered resistance R_3 of the specimens as achieved in Fig. 4(d)

	ZnO	ZnO/Ag_2S	ZnO/MoS_2	ZnO/MoS_2/Ag_2S
R_1 (Ω cm^2)	3.537	5.144	6.124	5.149
R_2 (Ω cm^2)	11.67	7.591	4.789	7.485
R_3 (Ω cm^2)	—	—	—	234.6

Table 2 Photodegradation efficiency of MB solution as catalyzed by the specimens in Fig. 4(e) and (f)

Light irradiation	ZnO	ZnO/Ag_2S	ZnO/MoS_2	ZnO/MoS_2/Ag_2S
UV	28.55%	31.91%	26.28%	58.12%
Visible	6.94%	17.24%	22.74%	52.88%

From practical point, keeping high photochemical activity and stability is a critical requirement for the catalysts. Therefore, the photocatalytic performance of the nanowire arrays was measured in three successive reaction periods, as displayed in Fig. S4,† and the efficiency was also computed and supplied in Table S1.† It is found that there is little variation in the peak intensity of the degradation solutions as catalyzed by the single and binary components, while the peak intensity improves obviously with increasing cycle for the ternary components. The distinct reduced efficiency may result from the losing of MoS_2 nanosheets and Ag_2S nanoparticles for the weak binding, or the surface covering of the degraded products. Nevertheless, the photocatalytic efficiency of ZnO/MoS_2/Ag_2S array retains larger than others in the UV light and visible light in any cycle. The stability of the ternary array was further tested by the photocatalytic performance under visible light in different conditions in Fig. S5 and Table S2 as well as the structure images in Fig. S6.† The catalytic efficiency of the specimen is found to nearly keep stable after 3 cycles. The efficiency of 25.30% in the 5th cycle is also larger than that of other samples in the 1st cycle under visible light. The nanorod array remains normal to the substrate after photocatalysis for 5 cycles. There is not clear difference in the array structure before and after photocatalytic performance, indicating a good photocatalytic stability of ZnO/MoS_2/Ag_2S array. Moreover, the efficiency increases with extending period and reaches 90.09% in 4 h. The MB solution is speculated to be degraded completely by the ternary array in about 5.5 h.

To make clear photocatalytic activity of the specimens, band structure of the heterogeneous interfaces is depicted in Fig. 5 based on the defect states in Fig. 4(b), bandgap (E_g) in Fig. S3,†

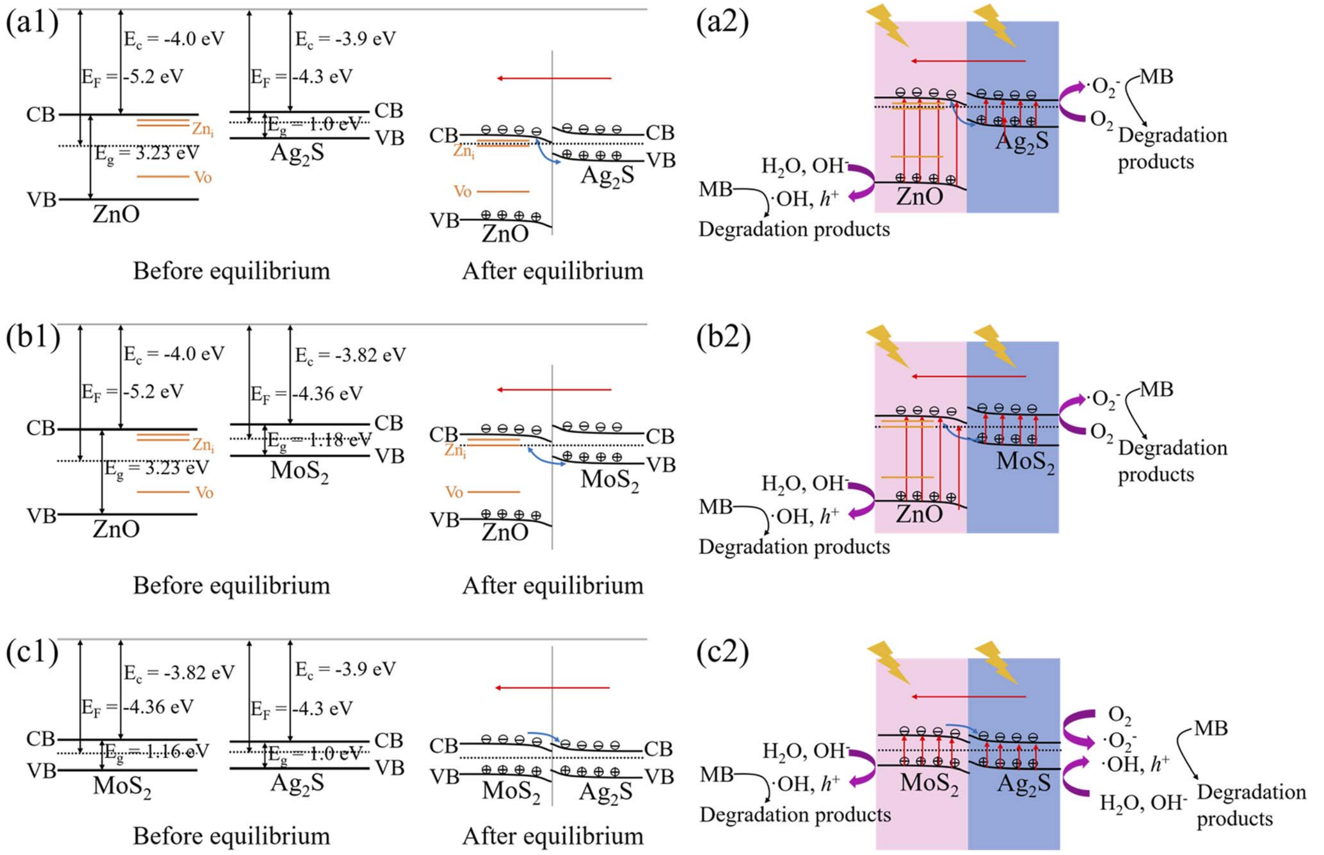

Fig. 5 Band diagrams and photocatalytic mechanisms of the heterogeneous nanorods at the interfaces: (a1, a2) ZnO/Ag_2S, (b1, b2) ZnO/MoS_2, (c1, c2) MoS_2/Ag_2S.

flat band potential (E_{FB}) in Mott–Schottky curves in Fig. S7,† work function (E_f) and electron affinity (E_C) of the semiconductor components in bulk state. For the ZnO–Ag_2S interface (see Fig. 5(a1)), the CB and VB of Ag_2S component straddle those of ZnO component, which forms a Type II heterojunction.[35] Since the absolute value of E_F for Ag_2S is smaller than that for ZnO, the Fermi level of Ag_2S is higher than that of ZnO. During formation of the internal electric field, the free electrons in Ag_2S flow to ZnO until the Fermi levels are aligned. Since the surface of ZnO is negatively charged while that of Ag_2S is positively charged, the direction of the internal electric field is from Ag_2S to ZnO, as indicated by a red arrow line. Therefore, the transfer of holes from Ag_2S to ZnO is favorable by the internal electric field, while the transfer of electrons in the same direction is prohibited. Meanwhile, the flow of photogenerated charge carriers in ZnO is opposite as that in Ag_2S, which results in the recombination of electrons in the CB of ZnO and holes in the VB of Ag_2S at the interface, as manifested by a blue arrow line. In addition, the shallow defects in Zn_i supply some seating states for the excited electrons. This particular Z-scheme energy diagram and extra states reduce charge recombination in the interior of the component semiconductors and improves redox ability of the heterojunction, which is beneficial for the photocatalytic performance. The Z-scheme diagram also exist in ZnO–MoS_2 interface, as shown in Fig. 5(b1). But for MoS_2–Ag_2S interface in Fig. 5(c1), the CB and VB of Ag_2S component seat in between those of MoS_2 component, which forms a Type I heterojunction. The internal electric field is from Ag_2S to MoS_2 as the work function of MoS_2 is larger than that of Ag_2S. As a result, the photoexcited electrons in the CB of MoS_2 flow to the CB of Ag_2S, while the carriers in other bands are restricted or gather at the interface for the energy barrier.

In light of the energy band structure, under light irradiation, the electrons in the VB of Ag_2S and ZnO are potentially excited to the CB and defect states. This Z-scheme heterojunction facilitates the residual holes in ZnO component to react with water molecules or hydroxide anion in the solution to produce $\cdot OH$ and h^+ species, while the excited electrons in Ag_2S component react with oxygen to generate $\cdot O_2^-$ species, all of which give rise to the decomposition of MB dyes, as illustrated in Fig. 5(a2). This process also occurs at the interfaces of ZnO–MoS_2 (see Fig. 5(b2)) heterojunctions. But for MoS_2–Ag_2S, the Type I heterojunction induces electrons in Ag_2S component to react with oxygen and generate $\cdot O_2^-$ species, while the holes in the two components bring $\cdot OH$ and h^+ species (see Fig. 5(c2)). All these lead to the dye degradation. In light of free radical trapping experiments (see Fig. S8 and Table S4†), the $\cdot OH$ and h^+ radicals play an important role in the degradation by the ternary ZnO/MoS_2/Ag_2S array. Therefore, the band alignment enhances photocatalytic performance of heterogeneous core–shell nanorod arrays. Especially for the ternary component ZnO/MoS_2/Ag_2S array, it contains both the staggered gap (Type II) of

ZnO–MoS_2 heterojunction in Fig. 5(b2) and straddling gap (Type I) of MoS_2–Ag_2S heterojunction in Fig. 5(c2), which extends the light absorption by the component semiconductors, reduces charge recombination efficiently by the energy barrier and band alignment, and possesses the highest active catalysis under visible light than ZnO/Ag_2S and ZnO/MoS_2 arrays. This may also have promising application in other fields, such as solar cells, photodiodes and photosensors.

4. Conclusions

ZnO-based nanorod arrays were successfully synthesized on the FTO substrate. The coating layers of MoS_2 nanosheets and Ag_2S quantum dots induced an intimate core–shell structure. In contrast to the single ZnO nanorod array, the binary and ternary semiconductor heterojunction arrays suppressed bandedge emission, improved light absorption, reduced resistance and increased photocatalysis. The ternary component ZnO/MoS_2/Ag_2S array possessed the highest active catalysis with an efficiency of 52.88% in 30 min under visible light, which was about 7.6 times that of ZnO array. Theory analysis revealed that the band alignment and extra states in the semiconductor heterojunctions played a critical role to reduce charge recombination and improve redox ability of the core–shell nanorod arrays, which was beneficial for the photocatalytic performance, and might also have promising applications in other fields such as varistors, photodiodes, and solar cells.

Author contributions

Jing Wan: prepared and characterized samples, analysed the data, discussed the results and wrote the original draft. Aseel Shaker Al-Baldawy: assisted on sample optimization and result discussion. Shanzhi Qu: performed optical and photocatalytic measurements. Jinshen Lan: performed SEM and TEM measurements. Xiaofang Ye: performed optical measurements. Yuchen Fei: assisted on sample optimization and result discussion. Jingtian Zhao: assisted on sample optimization and result discussion. Ziyun Wang: assisted on sample optimization and result discussion. Rongdun Hong: performed Raman measurement. Shengshi Guo: performed SEM measurement. Shengli Huang: conceptualized the idea, discussed the results, reviewed, edited the manuscript, supervised, and funded the project. Shuping Li: conceptualized the idea and discussed the results. Junyong Kang: conceptualized the idea and discussed the results.

Conflicts of interest

The authors declare that they have no known competing financial interests or personal relationships that could have appeared to influence the work reported in this paper.

Acknowledgements

This work was supported by the National Natural Science Foundation of China (61974125) and Natural Science Foundation of Jiangxi Province of China (20192ACBL20049).

References

1 F. Wang, Li Qi and D. Xu, Recent progress in semiconductor-based nanocomposite photocatalysts for solar-to-chemical energy conversion, *Adv. Energy Mater.*, 2017, **7**, 1700529.

2 A. Rafiq, M. Ikram, S. Ali, F. Niaz and M. Khan, Qasim Khan, Muhammad Maqbool, Photocatalytic degradation of dyes using semiconductor photocatalysts to clean industrial water pollution, *J. Ind. Eng. Chem.*, 2021, **97**, 111–128.

3 L. Zhang and M. Jaroniec, Toward designing semiconductor-semiconductor heterojunctions for photocatalytic applications, *Appl. Surf. Sci.*, 2018, **430**, 2–17.

4 H. R. Liu, G. X. Shao, J. F. Zhao, Z. X. Zhang, Y. Zhang, J. Liang, X. G. Liu, H. S. Jia and B. S. Xu, Worm-like Ag/ZnO core–shell heterostructural composites: fabrication, characterization, and photocatalysis, *J. Phys. Chem. C*, 2012, **116**, 16182–16190.

5 H. Qin, Y. Zuo, J. Jin, W. Wang, Y. Xu, L. Cui and H. Dang, ZnO nanorod arrays grown on g-C_3N_4 micro-sheets for enhanced visible light photocatalytic H_2 evolution, *RSC Adv.*, 2019, **9**, 24483–24488.

6 Y. Lin, S. Wu, C. Yang, M. Chen and Li Xiang, Preparation of size-controlled silver phosphate catalysts and their enhanced photocatalysis performance via synergetic effect with MWCNTs and PANI, *Appl. Catal., B*, 2019, **245**, 71–86.

7 Y. Lin, C. Yang, S. Wu, Li Xiang, Y. Chen and W. L. Yang, Construction of built-in electric field within silver phosphate photocatalyst for enhanced removal of recalcitrant organic pollutants, *Adv. Funct. Mater.*, 2020, **30**, 2002918.

8 R. Chen, S. Pang, H. An, J. Zhu, S. Ye, Y. Gao, F. Fan and C. Li, Charge separation via asymmetric illumination in photocatalytic Cu_2O particles, *Nat. Energy*, 2018, **3**, 655–663.

9 M. Hou, L. Cui, F. Su, X. Dong and H. Dang, Two-step calcination synthesis of Z-scheme α-Fe_2O_3/few-layer g-C_3N_4 composite with enhanced hydrogen production and photodegradation under visible light, *J. Chin. Chem. Soc.*, 2020, **67**, 2050–2061.

10 Y. Sun, Q. Zhao, J. Gao, Yu Ye, W. Wang, R. Zhu, J. Xu, Li Chen, J. Yang and L. Dai, Zhi-min Liao and Dapeng Yu, In situ growth, structure characterization, and enhanced photocatalysis of high-quality, single-crystalline ZnTe/ZnO branched nanoheterostructures, *Nanoscale*, 2011, **3**, 4418–4426.

11 Y. Xue, Z. Wu, X. He, X. Yang, X. Chen and Z. Gao, Constructing a Z-scheme heterojunction of egg-like core@shell CdS@TiO_2 photocatalyst via a facile reflux method for enhanced photocatalytic performance, *Nanomaterials*, 2019, **9**, 222.

12 H. Dang, S. Mao, Li Qi, M. Li, M. Shao, W. Wang and Q. Liu, Synergy of nitrogen vacancies and partially broken hydrogen bonds in graphitic carbon nitride for superior photocatalytic hydrogen evolution under visible light, *Catal. Sci. Technol.*, 2022, **12**, 5032–5044.

13 D. Ayodhya and G. Veerabhadram, A review on recent advances in photodegradation of dyes using doped and

heterojunction based semiconductor metal sulfide nanostructures for environmental protection, *Mater. Today Energy*, 2018, **9**, 83–113.

14 R. Ganatra and Q. Zhang, Few-layer MoS_2: a promising layered semiconductor, *ACS Nano*, 2014, **8**, 4074–4099.

15 J. Xue, J. Liu, Y. Liu, H. Li, Y. Wang, D. Sun, W. Wang, L. Huang and J. Tang, Recent advances in synthetic methods and applications of Ag_2S-based heterostructure photocatalysts, *J. Mater. Chem. C*, 2019, **7**, 3988–4003.

16 C. Ding, Y. Huang, Z. Shen and X. Chen, Synthesis and bioapplications of Ag_2S quantum dots with near-infrared fluorescence, *Adv. Mater.*, 2021, **33**, 2007768.

17 J. Lan, M. Gao, C. Haw, I. Khan, J. Zhao, Z. Wang, S. Guo, S. Huang, S. Li and J. Kang, Layer-by-layer assembly of Ag_2S quantum dots-sensitized ZnO/SnO_2 core-shell nanowire arrays for enhanced photocatalytic activity, *Phys. Lett. A*, 2020, **384**, 126708.

18 W. Jian, X. Cheng, Y. Huang, Yu You, Ru Zhou, T. Sun and J. Xu, Arrays of ZnO/MoS_2 nanocables and MoS_2 nanotubes with phase engineering for bifunctional photoelectrochemical and electrochemical water splitting, *Chem. Eng. J.*, 2017, **328**, 474–483.

19 D. Solís-Cortés, F. Martín Jiménez, G. Jauregui, D. Gau, J. Pereyra, H. Rodrigo, R. E. Marotti, J. R. Ramos-Barrado and E. A. Dalchiele, Optimization of Ag_2S quantum dots decorated ZnO nanorod array photoanodes for enhanced photoelectrochemical performances, *J. Electrochem. Soc.*, 2021, **168**, 056516.

20 S. Chen, F. Liu, M. Xu, J. Yan, F. Zhang, Z. Wu, Z. Zhang, Z. Deng, J. Yun, R. Chen and C. Liu, First-principles calculations and experimental investigation on SnO_2@ZnO heterojunction photocatalyst with enhanced photocatalytic performance, *J. Colloid Interface Sci.*, 2019, **553**, 613–621.

21 D. Ju, H. Xu, Z. Qiu, Z. Zhang, Xu Qi, J. Zhang, J. Wang and B. Cao, Near room temperature, fast-response, and highly sensitive triethylamine sensor assembled with Au-loaded ZnO/SnO_2 core–shell nanorods on flat alumina substrates, *ACS Appl. Mater. Interfaces*, 2015, **7**, 19163–19171.

22 Md. Tamez Uddin, Y. Nicolas, C. Olivier, T. Toupance, L. Servant, M. M. Muller, H.-J. Kleebe, J. Ziegler and W. Jaegermann, Nanostructured SnO_2 - ZnO heterojunction photocatalysts showing enhanced photocatalytic activity for the degradation of organic dyes, *Inorg. Chem.*, 2012, **51**, 7764–7773.

23 X. Li, D. Liu, Z. Shi and J. Yang, Effect of Ag_2S shell thickness on the photocatalytic properties of ZnO/Ag_2S core–shell nanorod arrays, *J. Mater. Sci.*, 2019, **54**, 1226–1235.

24 G. Eda, H. Yamaguchi, D. Voiry, T. Fujita, M. Chen and M. Chhowalla, Photoluminescence from chemically exfoliated MoS_2, *Nano Lett.*, 2011, **11**, 5111–5116.

25 V. Putritama, V. Fauziaa and A. Supangat, The effect of the layer number of MoS_2 nanosheets on the photocatalytic efficiency of ZnO/MoS_2, *Surf. Interfaces*, 2020, **21**, 100745.

26 H. Li, H. Shen, L. Duan, R. Liu, Q. Li, Q. Zhang and X. Zhao, Enhanced photocatalytic activity and synthesis of ZnO nanorods/MoS_2 composites, *Superlattice. Microst.*, 2018, **117**, 336–341.

27 Q. Yang, D. Li, B. Yu, S. Huang, J. Wang, S. Li and J. Kang, Size effect on morphology and optical properties of branched ZnO/Si nanowire arrays, *Phys. Lett. A*, 2016, **380**, 1044–1048.

28 H. Zeng, G. Duan, Li Yue, S. Yang, X. Xu and W. Cai, Blue luminescence of ZnO nanoparticles based on non-equilibrium processes: defect origins and emission controls, *Adv. Funct. Mater.*, 2010, **20**, 561–572.

29 W. C. Zhang, X. L. Wu, H. T. Chen, J. Zhu and G. S. Huang, Excitation wavelength dependence of the visible photoluminescence from amorphous ZnO granular films, *J. Appl. Phys.*, 2008, **103**, 093718.

30 H. Dua, Y. Kang, C. Xu, T. Xue, W. Qiu and H. Xie, Measurement and characterization of interfacial mechanical properties of graphene/MoS_2 heterostructure by Raman and photoluminescence (PL) spectroscopy, *Opt Laser. Eng.*, 2022, **149**, 106825.

31 M. Jasna, M. M. Pillai, A. Abhilash, P. S. Midhun, S. Jayalekshmi and M. K. Jayaraj, Polyaniline wrapped carbon nanotube/exfoliated MoS_2 nanosheet composite as a promising electrode for high power supercapacitors, *Carbon Trends*, 2022, **7**, 100154.

32 K. Rahimi, M. Moradi, R. Dehghan and Y. Ahmad, Enhancement of sunlight-induced photocatalytic activity of ZnO nanorods by few-layer MoS_2 nanosheets, *Mater. Lett.*, 2019, **234**, 134–137.

33 S. Khanchandani, S. Kundu, A. Patra and A. K. Ganguli, Band gap tuning of ZnO/In_2S_3 core/shell nanorod arrays for enhanced visible-light-driven photocatalysis, *J. Phys. Chem. C*, 2013, **117**, 5558–5567.

34 Ya N. Wang, Li Jin and Q. Wang, The performance of daylight photocatalytic activity towards degradation of MB by the flower-like and approximate flower-like complexes of graphene with ZnO and cerium doped ZnO, *Optik*, 2020, **204**, 164131.

35 H. Zhou, Y. Qu, T. Zeid and X. Duan, Towards highly efficient photocatalysts using semiconductor nanoarchitectures, *Energy Environ. Sci.*, 2012, **5**, 6732.